Supplemental Material for

Making Patterned Single Defects in MoS_2 Thermally with the MoS_2/Au Moiré Interface

Yang Bao, Hai Xu, Jia-Xu Yan, Peng-Tao Jing, Ji-Lian Xu, Da Zhan, Lei Liu*, De-Zhen Shen*

State Key Laboratory of Luminescence and Applications, Changchun Institute of Optics, Fine Mechanics and Physics, Chinese Academy of Sciences, No. 3888 Dongnanhu Road, Changchun 130033, People's Republic of China

*Corresponding author. Email: liulei@ciomp.ac.cn ; shendz@ciomp.ac.cn

This file includes

Materials and Methods

Sec. M1. Molecular Beam Epitaxy (MBE) growth of MoS_2 Films on Au(111):

The MoS_2 thin film was grown in an ultrahigh vacuum (UHV, base pressure=1×10^{-10}mbar) chamber by molecular beam epitaxy. The Au(111) growth substrate was cleaned by multiple sputtering (argon pressure=1×10^{-5}mbar, beam energy=1.5keV) and annealing cycles. Molybdenum (Mo) was deposited onto the clean Au (111) surface by e-beam evaporator (Focus GmbH, ion flux= 2 nA, deposition time = 40 min). Subsequently, the chamber was backfilled with H_2S gas (5×10^{-6} mbar) while keeping the substrate temperature at 200°C for 40min, in order to facilitate the complete conversion of metallic Mo into small domain MoS_2. This procedure is helpful to avoid the formation of Au-Mo alloys that may negatively affect the formation of atomically sharp MoS_2/Au moiré interfaces. Next, while keeping the H_2S pressure unchanged, the growth temperature was raised to 450°C for 20min to merge the small domain MoS_2 into larger MoS_2 islands. Finally, H_2S dosage was stopped, and the sample was kept at 450°C for another 10min to desorb the surface sulfur adatoms, before cooling down to room temperature. Our observation of the sulfur desorption temperature is consistent with values reported in the literature [1]. The sample temperatures used throughout this paper are nominal temperatures measured from a thermal couple that is attached near the sample heating stage. The real sample temperature would be higher by about 50°C as compared to the nominal temperature according to the calibration curve provided by the supplier (Omicron GmbH).

Sec. M2. Defect creation and STM characterizations:

The as-grown MoS_2 samples were annealed in UHV at 500°C, 520°C and 580°C (nominal temperature) for 40 min to induce the formation of thermally-activated defects. The defect density can be controlled by changing the annealing time. For the defect creation via ion sputtering, the sputter gun was aligned in the perpendicular direction of the sample surface, the chamber was backfilled with argon (Ar) gas (2×10^{-8} mbar) and the beam energy was set to 200eV, the ion flux can be inferred from the sputter current (around 7 μA) between sample and the ground, the sample was kept at room temperature during sputtering. These parameters were the threshold parameters to induce defect formation: lower beam energies or argon pressures will

barely change the STM topography of the MoS_2 sample, and higher parameters will obviously give rise to higher defect densities and more complex defect structures.

After the defect creation via the above methods, the samples were transferred into the analysis chamber with a base pressure of 5×10^{-11}mbar, and STM was performed at 4.5K with electrochemically etched tungsten tips (Omicron GmbH). Scanning tunneling spectroscopy (STS) was performed with a lock-in amplifier (Stanford Research Systems) by applying an AC modulation with an amplitude of 5mV at a frequency of 335.7Hz to the DC bias voltage, all STS spectra were obtained with a single sweep to minimize the thermal drift effect that changes the tip position.

Sec. M3. Density functional theory (DFT) simulation methods for STM and phonon-related properties:

All calculations are performed based on the DFT with the Vienna *ab initio* simulation package (VASP) [2] using the projector augmented wave method [3,4]. The exchange-correlation functional proposed by Perdue, Burke, and Ernzerhof (PBE) [5] was adopted. Taking account of nonlocal van der Waals interaction, we adopted the newly developed vdW density functional (optB86b-vdW) [6]. The energy convergence for the relaxation (with and without defects) was chosen to be less than 10^{-4} eV/Å and the Brillouin zone was sampled by a 3×3×1 k-point mesh. Considering the moiré pattern observed in the experiment, we constructed 11×11 MoS_2 on a 12×12 three-layer Au (111) substrate as a slab model (11-on-12 model) with a vacuum layer of at least 10 Å to avoid unphysical interactions between replica of the slab models. It is noteworthy that the native herringbone reconstruction of the Au (111) surface beneath the MoS_2 islands are likely lifted as suggested by several reports [7-9], hence a bulk-terminated Au lattice was used in constructing the structural model of the moiré superlattice. In some reports [10], a 10-on-11 commensurate model was also used to describe the moiré superstructure. While both models are legitimate as commensurate approximations of the MoS_2/Au (111) moiré superstructure, we used the 11-on-12 model since it better matches our atom-resolved STM images. To obtain a visual description of the influence of the defects, we constructed the S vacancy models located in the upper layer and lower layer and then performed STM simulations using the Tersoff-Hamann approach [11]. The phonon-related properties of the moiré cell were calculated using finite

differences as deployed in Phonopy [12]. Firstly, the dynamical force constants for the supercell including 795 atoms at the zone center were computed. We then unfolded the Bloch wave from supercell to primitive cell and obtained the phonon spectral functions [13]. The spatial distributions of the MoS_2 out-of-plane acoustic (ZA) mode were also interpolated by vibrational amplitudes of the MoS_2 layer.

Sec. M4. Defect formation energy and reaction barrier calculations:

We employed the DFT calculations as implemented in the CP2K Quickstep package [14]. We utilized the Goedecker-Teter-Hutter pseudopotentials [15,16] for core electrons, and double-zeta polarized basis sets for valence electrons. These selections effectively modeled the core and valence electrons. The energy cutoffs were set at 300 Ry for the finest grid level and 40 Ry for Gaussian waves. To account for dispersion interactions, we employed the Grimme dispersion correction method [17,18]. The GGA PBE functional [5] was used to describe electronic exchange-correlation effects. The MoS_2 on Au (111) is simulated superimposing a 11×11 MoS_2 supercell on a 12 × 12 Au (111). The metal substrate is modelled as a four-layer slab, where the atoms of the bottom layer are kept fixed to their bulk position during the relaxation. The formation energy E_f of a S vacancy is calculated as $E_f = E_{total}[\text{vac}] - E_{total}[\text{pristine}] + \mu_s$. Here $E_{total}[\text{vac}]$ and $E_{total}[\text{pristine}]$ are the total energy of the system (at T = 0) with and without a vacancy, respectively. μ_s is the reference chemical potential for S atom (that of S crystal in this study). The reaction/migration barriers of the sulfur atom across various diffusion pathways were calculated employing the climbing image nudged elastic band (CI-NEB) method [19]. For each of the diffusion pathways investigated, twelve replicas/images were utilized. The technique of direct inversion in the iterative subspace (DIIS) was employed [20]. Visualization of these interactions was achieved using the VESTA software [21].

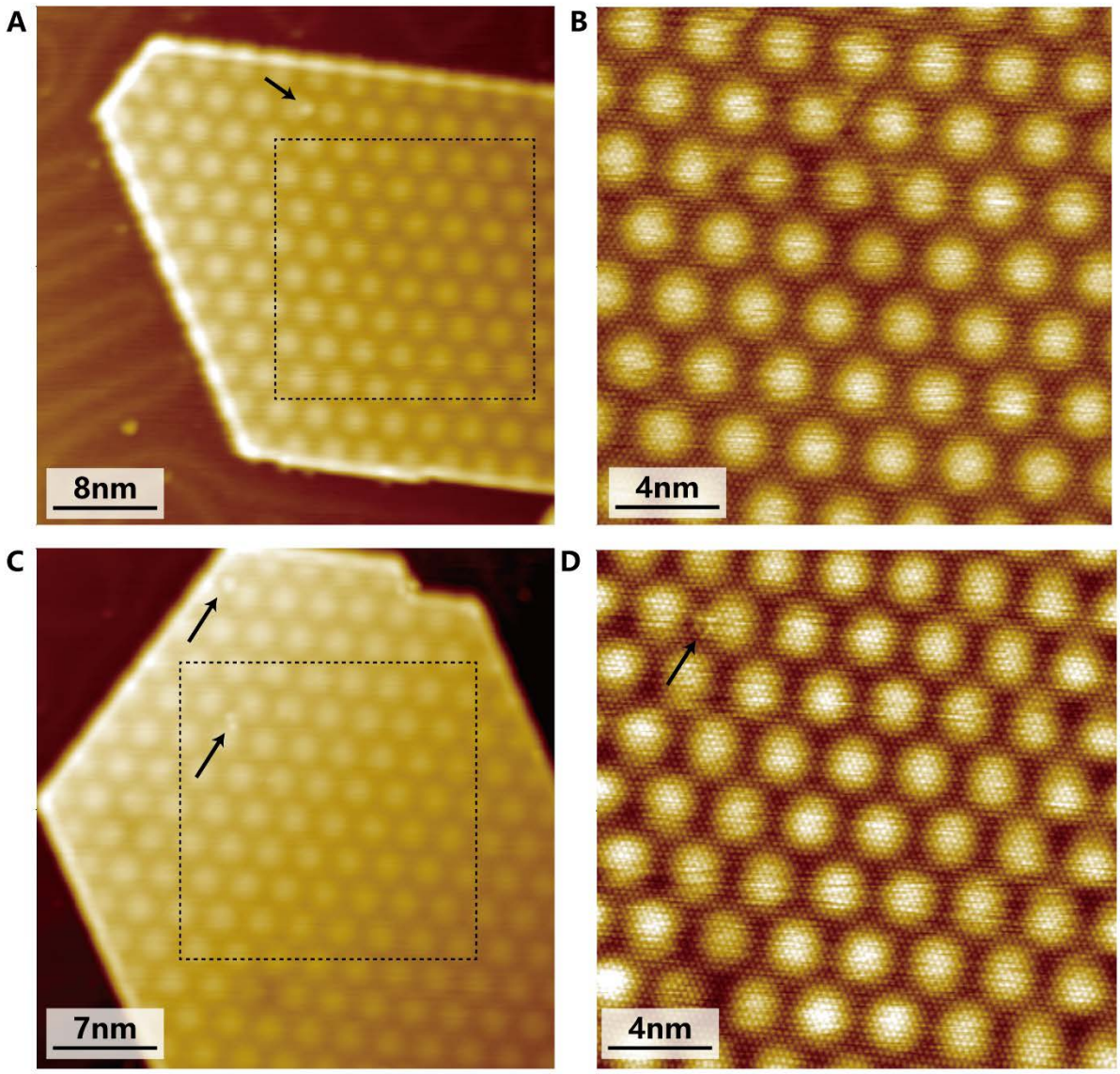

fig. S1. The low intrinsic defect density of the as-grown MoS_2 samples. (A, B) STM images of the as-grown MoS_2 islands, with an average size of about 40nm x 40nm. For each island, we typically image 1-2 intrinsic defects, corresponding to an estimated defect density of about 1×10^{11} to 2×10^{11} cm^{-2}. This value is at least one order of magnitude smaller than the defect densities of the mechanically exfoliated MoS_2 films (~$1\times 10^{13} cm^{-2}$) [22], allowing us to easily distinguish the post-growth engineered defects from intrinsic ones. **(C, D)** atom-resolved STM images of the region enclosed by dashed box in **A** and **B**, respectively.

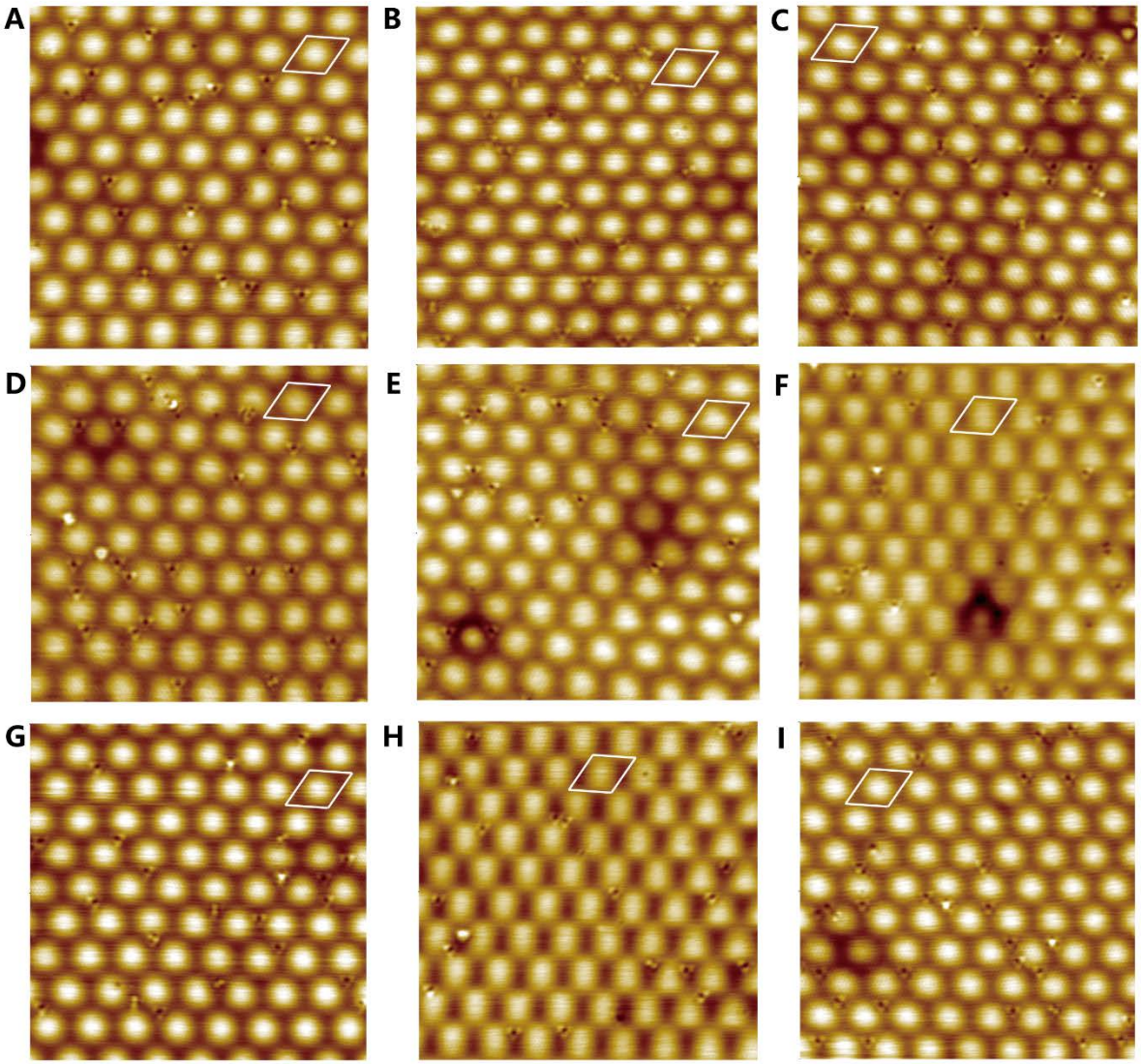

fig. S2. Large-scale STM images used for the statistical analysis of the defect distribution, obtained with the MoS_2 samples annealed at 500℃ for 40min. In each image, the moiré supercell was labelled by a solid diamond. Size of each image is 25nmx25nm, STM imaging parameter: U=-300mV, I=1nA. In these images, some depression regions are occasionally observed in the MoS_2 layer for certain unknown reason. Apparently, such depressions do not affect the preferential localization of the single defects at the hollow moiré regions.

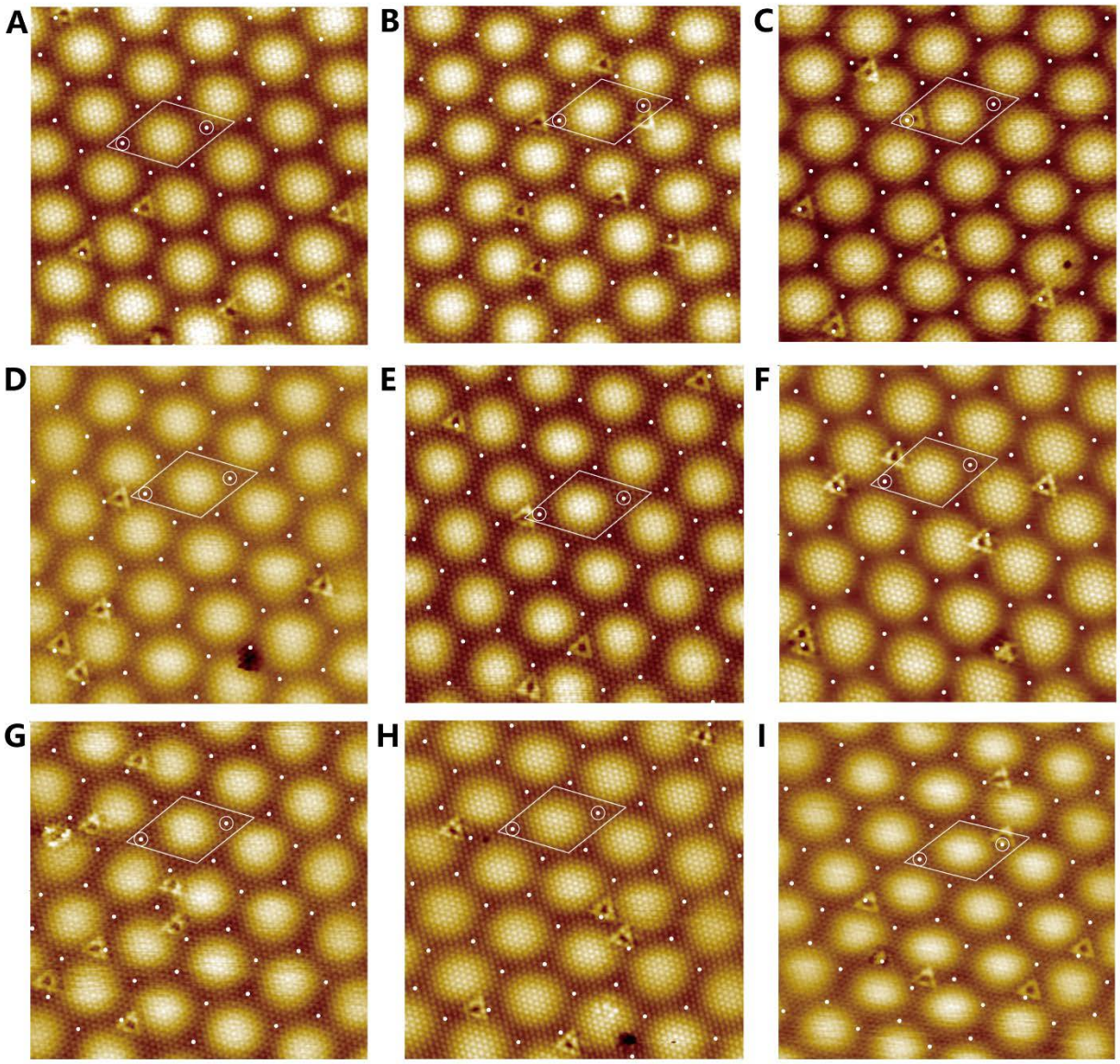

fig. S3. Atom-resolved STM images used for counting the defect distribution and the defect distance to the centers of the hollow moiré regions, obtained with the MoS_2 samples annealed at 500℃ for 40min. In each image, the moiré supercell was labelled by a solid diamond, and the centers of the hollow moiré regions were marked by white dots. Size of each image is 15nmx15nm, STM imaging parameters: U=-10mV, the current (I) ranges from 40nA to 80nA depending on the condition of the tip apex.

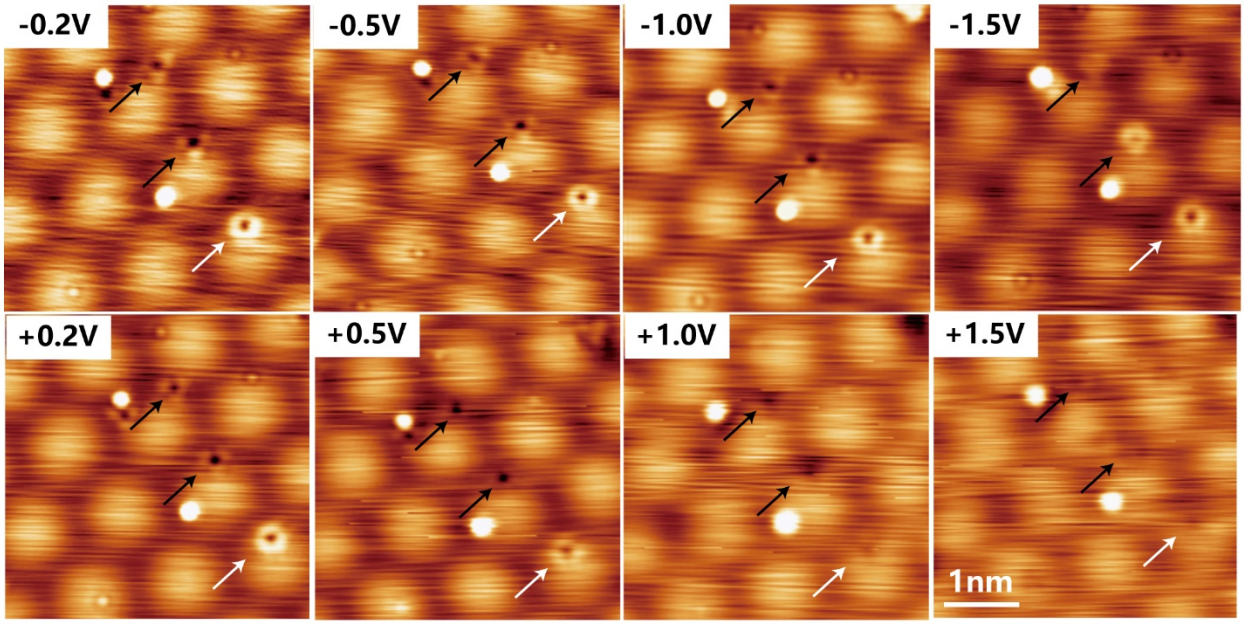

fig. S4. Bias-dependent STM images of the V_S-int and V_S-surf single defects in MoS_2. In these images captured at the same position, two Vs-int defects are indicated by black arrows, and one V_S-surf defect is indicated by a white arrow. The triangular-shaped topography of the Vs-int defect, and the trigonal-ring-shaped topography of the Vs-surf defect are consistently imaged in the range of -1.5V to +0.2V. From +0.5V to +1.5V, the defects become less visible in their STM contrast, probably because the tunneling current is predominantly contributed by the electronic states of the host (i.e. MoS_2) and the substrate (i.e. Au), instead of the defect states.

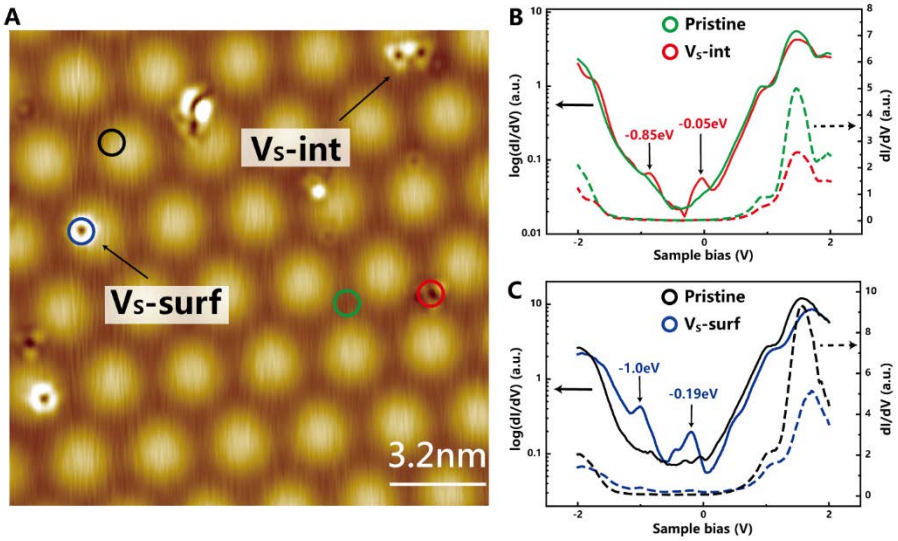

fig. S5. dI/dV spectra of the V_S-int and V_S-surf single defects in MoS_2. (**A**) STM image of the region containing both types of the prolific single defects, with colored circles corresponding to the positions where the dI/dV spectra were collected. (**B**) The dI/dV spectra of the V_S-int defect (red) comparing to dI/dV of the pristine MoS_2 region (green). (**C**) The dI/dV spectra of the V_S-surf defect (blue) comparing to dI/dV of the pristine MoS_2 region (black). All spectra were plotted in both the linear (dashed curves) and the logarithmic (solid curves) scale.

The electronic states of the prolific single defects were studied by scanning tunnelling spectroscopy (STS). **fig. S5B** depicts the STS spectra of the V_S-int defect, in which the onsets of valence and conduction bands are similar to that of the pristine MoS_2. The defect-induced features are not obvious in the linear-scale spectrum (dashed line), probably due to the substrate screening effect. After plotting the spectrum in logarithmic scale (solid line), two defect-related peaks at -0.85eV and -0.05eV are visible. The -0.05eV peak is about 550meV below the conduction band minimum (CBM), matching well with the previously calculated deep in-gap state of the V_S defect in MoS_2 [23]. The origin of the -0.85eV peak is currently unknown, which could be temporarily assigned as an interface electronic state. Similarly, in the STS spectrum of the V_S-surf defect (**fig. S5C**), two peaks at -1.0eV and -0.19eV were observed, which were rigidly shifted by ~0.15eV compared to the V_S-surf defect states. This rigid shift reflects the different of the local work functions at the two defect sites, which will be explained in **fig. S6**.

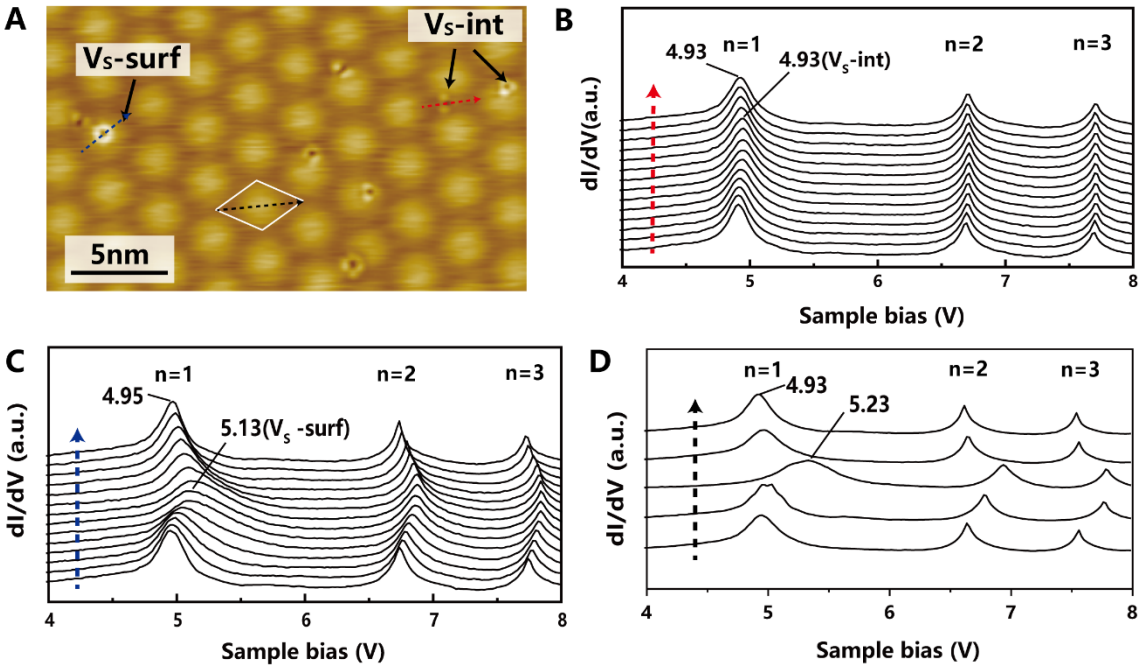

fig. S6. Field emission resonance (FER) spectra of the V_S-int and V_S-surf defect sites. (A) STM image showing both the V_S-int and V_S-surf defects, red and blue dash lines mark the positions where constant current dI/dV spectra (i.e. the FER spectra) were acquired. **(B, C)** Field emission resonance (FER) spectra taken along a line across the V_S-surf defect and the V_S-int defect, respectively. **(D)** Field emission resonance (FER) spectra taken at five points across a defect free top moiré region (positions marked by the black dash line). As the FER states are analogous to the electronic states of the hydrogen atom, we use the primary quantum number n to denotes them, with n=1 corresponding to the ground state, n=2 to the first excited state, etc.

In the STS spectra of the surface and interface sulfur mono-vacancy defects (see **fig. S5**), their defect states were rigidly shifted by about 0.15eV. This can be explained the fact that the V_S-surf defect is located at a top moiré region, whereas the V_S-int defect is at a hollow moiré region. Due to the different amount of interfacial charge transfer between these two moiré regions, different local work functions are expected at the two defect sites. The local work functions can be probed by field emission resonance (FER) measurements. FER occurs in the case when the applied bias in the tunneling junction is higher than the sample work function, that is, the Fermi level of the tip is higher than the vacuum level of the sample. Consequently, the potential drop between tip and sample will give rise to hydrogen like electron resonances

confined in the tunneling junction, which appear as sharp peaks in the constant current dI/dV spectra [24]. The onset bias of the first FER peak roughly corresponds to the local work function. Here we acquired a series of constant current dI/dV spectra taken across the V_S-int and V_S-surf defects (indicated by red and blue dashed lines in **fig. S6A**, respectively). While the V_S-int defect has a similar work function of 4.93eV with that of the pristine MoS_2 regions (**fig. S6B**), the work function of the V_S-surf defect is shifted by about 0.2eV (**fig. S6C**). The measured work function difference between the V_S-int and V_S-surf defects (0.2eV) is comparable to the shift in their STS peaks (0.15eV). A reference measurement was performed at five points across a defect free top moiré region (**fig. S6D**), showing a work function shift of about 0.3eV at the TOP moiré site, as compared to the hollow sites.

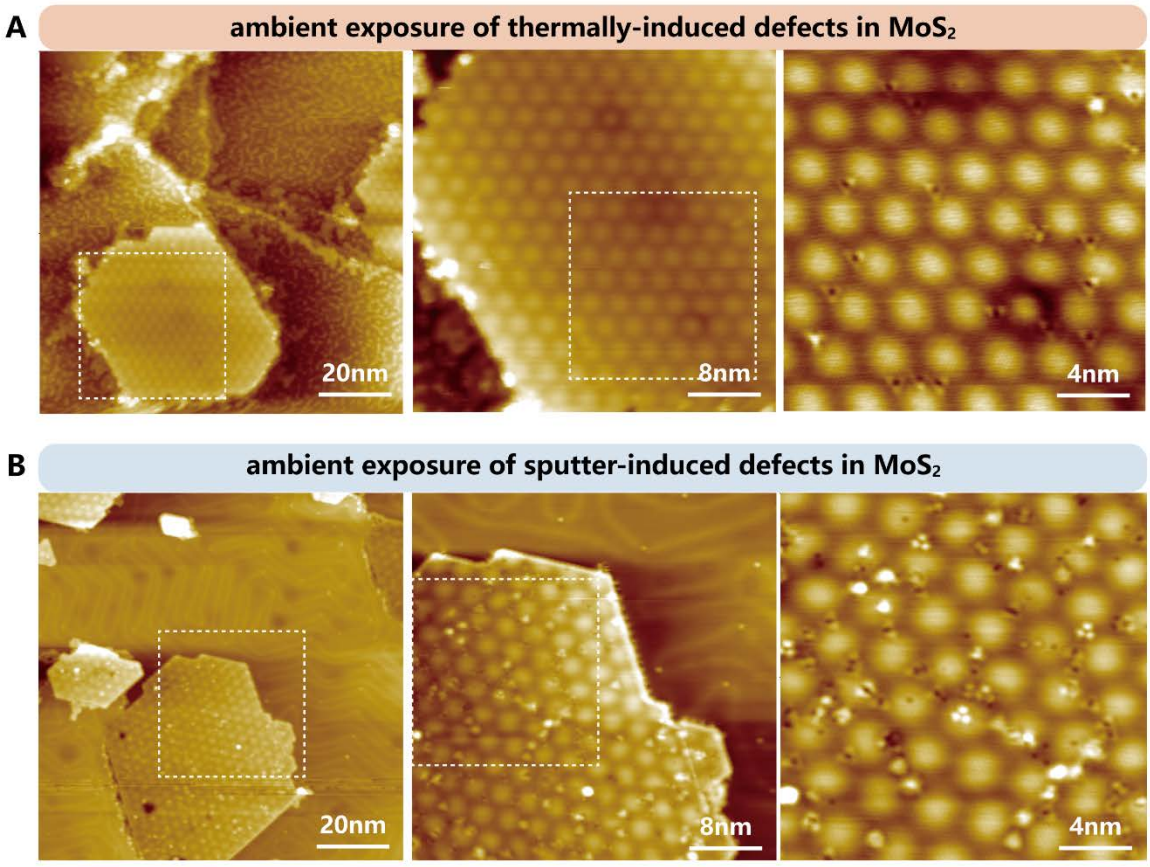

fig. S7. Ambient stability of the interface (V_S-int) and surface (V_S-surf) sulfur vacancies. (A) A serious of zoomed-in STM images of the MoS_2 surface, taken after 2h of air exposure of the thermally-annealed MoS_2 sample. The thermally-induced triangular shaped defects, that is the V_S-int defects, remain unchanged after air exposure. **(B)** A serious of zoomed-in STM images of

the MoS_2 surface, taken after 30min of air exposure of the ion-sputtered MoS_2 sample. STM imaging reveals the absence of trigonal-ring shaped defects (i.e. the V_S-surf defects), indicating they were chemically converted to other structures upon air exposure.

The ambient stability of the V_S-int and V_S-surf defects were evaluated by performing ambient exposure experiments of the MoS_2 samples treated by thermal annealing and ion sputtering, respectively. The thermally-annealed (500℃, 40min) MoS_2 sample was exposed to air for 2h, and then annealed in UHV at 300℃ for another 2h to remove physiosorbed impurities such as water and hydrocarbons. STM images of the sample (**fig. S7A**) revealed that the bare Au surface region was covered by a high density of irregular adsorbents which were likely hydrocarbons from the air. In contrast, the MoS_2 domains remain free of adsorbents, suggesting the weakly interacting hydrocarbons were thermally desorbed from the dangling-bond free MoS_2 surface. Atom-resolved STM image revealed the characteristic triangular-shaped STM contrast of the V_S-int defects, suggesting these defects were unaffected by air exposure. In contrast, for the argon ion sputtered MoS_2 sample, V_S-surf defects with the characteristic trigonal-ring-shaped STM topography were no longer observed (**fig. S7B**). This is likely due to the oxidation of the V_S-surf defects during air exposure, which convert them into the top-layer oxygen substitutional (O_S-surf) defects [25]. These results demonstrate the excellent ambient stability of the thermally-induced single defects in MoS_2, which are located at the interface and hence protected by the substrate encapsulation. This means they can serve as robust quantum point defects without the need of further protection, for the construction of ambient stable classical or quantum devices.

A

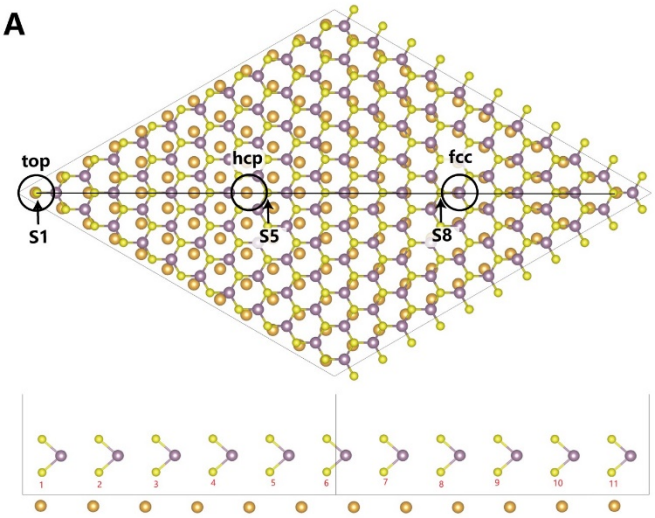

B

Index of interface S atom	Distance to the nearest Au atom (Å)	Distance to the Au surface plane (Å)	Distance to the Au surface plane (Å) as in ref. 9.
S1 (TOP)	2.52050	2.52050	2.53
S2	2.53914		
S3	2.64602		
S4	2.95493		
S5 (HCP)	3.35709	2.780625	2.73
S6	3.65319		
S7	3.57429		
S8 (FCC)	3.32549	2.742125	2.69
S9	2.52050		
S10	2.53914		
S11	2.64602		

fig. S8. (**A**) Upper panel: Top view of the 11-on-12 MoS_2/Au(111) moiré supercell, with the top, hcp and fcc sites circled accordingly. Lower panel: Side view of the interface S-Au registry cut along the long diagonal of the moiré supercell, with each bottom S atoms labelled by numbers. The 11-on-12 model was relaxed to minimize the total energy of the system, with the energy convergence for the relaxation chosen to be less than 10-4 eV/Å. Atom S1, S5 and S8 refers to the bottom S atom at the TOP, HCP and FCC moiré site, respectively. (**B**) For each of the bottom S atom, its distance to the nearest surface Au atom, as well as its height with respect to the Au surface plane, are listed in the table. In both cases, the shortest S-Au atom distance or S-Au plane distance is observed at the TOP moiré site. This analysis is in line with previous reports, all concluded that the MoS_2 layer has the lowest height (or shortest S-Au distance) at the TOP moiré sites. [10,26,27]

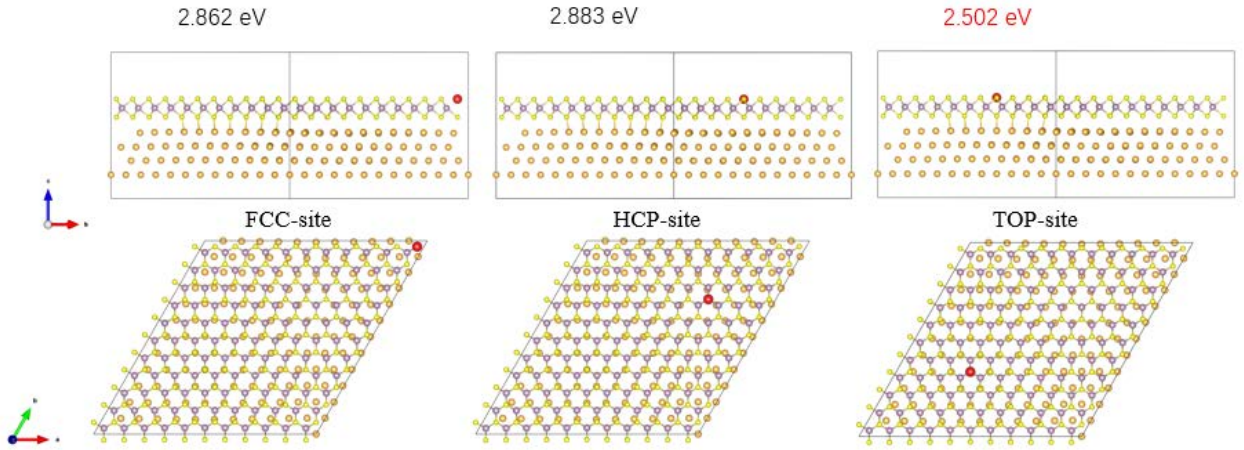

fig. S9. The calculated formation energy of V_S defects at various surface sites. The red ball denotes the position of the S vacancy, with the configuration exhibiting the lowest energy highlighted in red. The depiction offers a simplified top view, showcasing only a single layer of gold atoms. The relative trend in our results is comparable to a previous study[10], which reported the V_S-surf formation energies as 2.81 eV, 3.01 eV and 3.04 eV, at the TOP site, HCP site and FCC site, respectively.

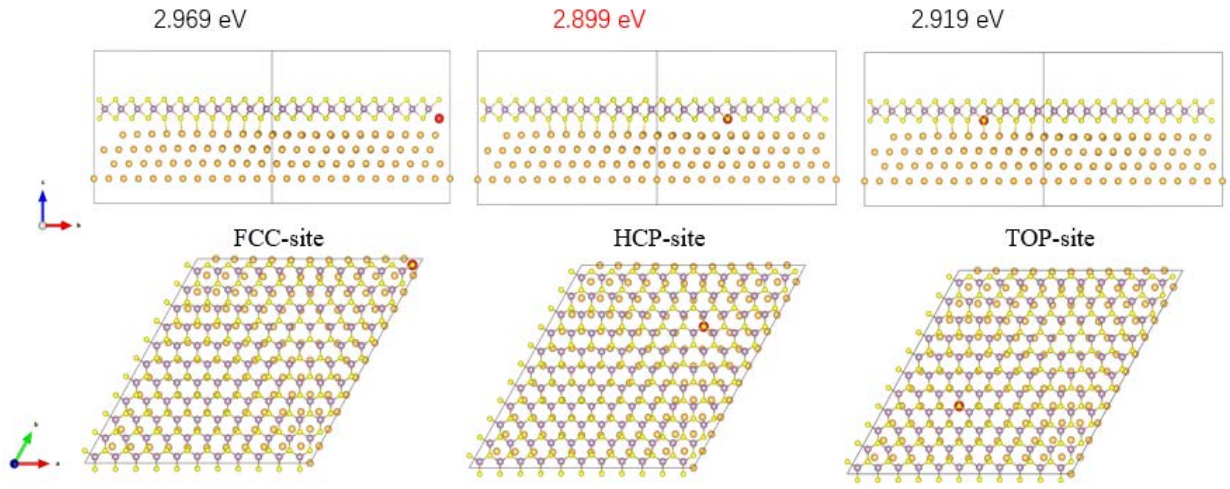

fig. S10. The calculated formation energy of V_S defects at various interface sites. The red ball denotes the position of the S vacancy, with the configuration exhibiting the lowest energy highlighted in red. The depiction offers a simplified top view, showcasing only a single layer of gold atoms. The relative trend in our results is comparable to a previous study [10], which reported the V_S-int formation energies as 3.00 eV, 3.17 eV and 3.13 eV, at the HCP site, FCC site and TOP site, respectively.

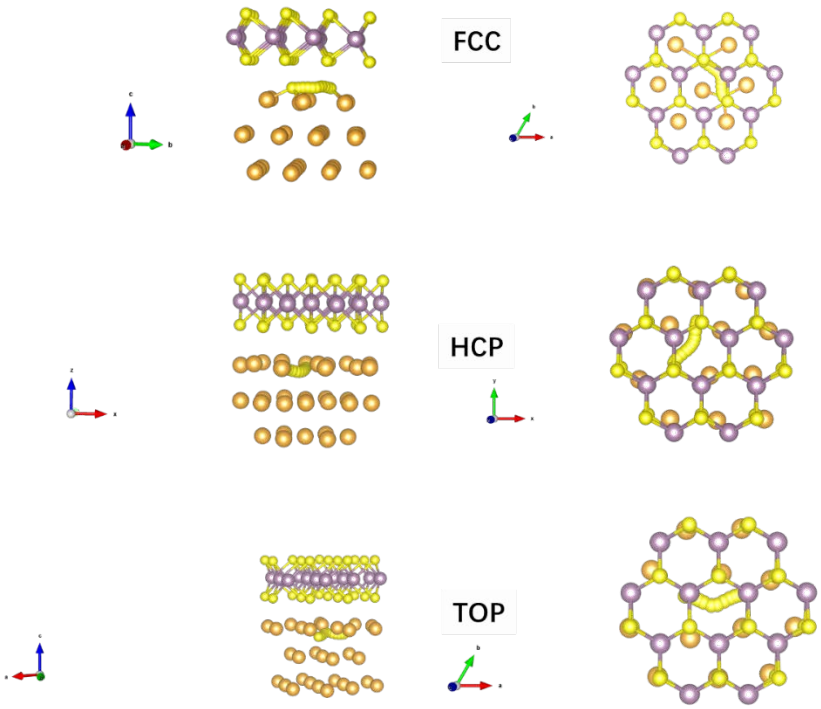

fig. S11. The representative CI-NEB images for the intercalated S atom migrating within the S-Au interface, starting from various moiré sites (FCC, HCP and TOP) to reach a nearby metastable site, along the minimum energy reaction pathway.

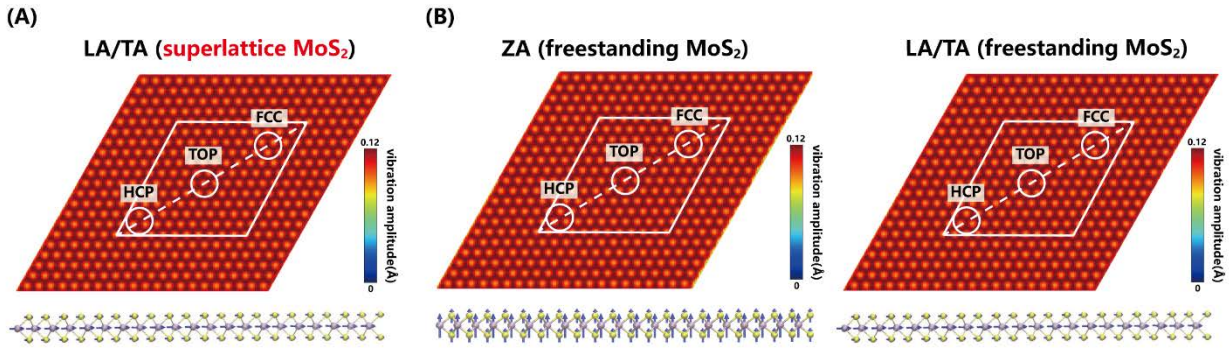

fig. S12. (**A**) Upper panel: Real-space distribution of the vibration amplitude in the superlattice MoS_2 for its LA/TA phonons. Lower panel: Side view of the vibration amplitude (represented by the length of the blue arrows), cut along the long diagonal of the (11x11)-MoS_2 supercell (dashed line in solid rhombus). (**B**) Upper panel: Real-space distribution of the vibration amplitude in the freestanding MoS_2, for its ZA and LA/TA phonons respectively. Lower panel: Side view of the corresponding vibration amplitude (represented by the length of the blue arrows), cut along the long diagonal of the (11x11)-MoS_2 supercell (dashed line in solid rhombus).

References

1 Rodriguez, J. A. *et al.* Coverage Effects and the Nature of the Metal−Sulfur Bond in S/Au(111): High-Resolution Photoemission and Density-Functional Studies. *Journal of the American Chemical Society* **125**, 276-285, doi:10.1021/ja021007e (2003).

2 Kresse, G. & Furthmüller, J. Efficient iterative schemes for ab initio total-energy calculations using a plane-wave basis set. *Physical Review B* **54**, 11169-11186, doi:10.1103/PhysRevB.54.11169 (1996).

3 Kresse, G. & Joubert, D. From ultrasoft pseudopotentials to the projector augmented-wave method. *Physical Review B* **59**, 1758-1775, doi:10.1103/PhysRevB.59.1758 (1999).

4 Blöchl, P. E. Projector augmented-wave method. *Physical Review B* **50**, 17953-17979, doi:10.1103/PhysRevB.50.17953 (1994).

5 Perdew, J. P., Burke, K. & Ernzerhof, M. Generalized Gradient Approximation Made Simple. *Physical Review Letters* **77**, 3865-3868, doi:10.1103/PhysRevLett.77.3865 (1996).

6 Klimeš, J., Bowler, D. R. & Michaelides, A. Van der Waals density functionals applied to solids. *Physical Review B* **83**, 195131, doi:10.1103/PhysRevB.83.195131 (2011).

7 Krane, N., Lotze, C. & Franke, K. J. Moiré structure of MoS2 on Au(111): Local structural and electronic properties. *Surface Science* **678**, 136-142, doi:https://doi.org/10.1016/j.susc.2018.03.015 (2018).

8 Grønborg, S. S. *et al.* Synthesis of Epitaxial Single-Layer MoS2 on Au(111). *Langmuir* **31**, 9700-9706, doi:10.1021/acs.langmuir.5b02533 (2015).

9 Sørensen, S. G., Füchtbauer, H. G., Tuxen, A. K., Walton, A. S. & Lauritsen, J. V. Structure and Electronic Properties of In Situ Synthesized Single-Layer MoS2 on a Gold Surface. *ACS Nano* **8**, 6788-6796, doi:10.1021/nn502812n (2014).

10 Tumino, F., Casari, C. S., Li Bassi, A. & Tosoni, S. Nature of Point Defects in Single-Layer MoS2 Supported on Au(111). *The Journal of Physical Chemistry C* **124**, 12424-12431, doi:10.1021/acs.jpcc.0c01477 (2020).

11 Tersoff, J. & Hamann, D. R. Theory of the scanning tunneling microscope. *Physical Review B* **31**, 805-813, doi:10.1103/PhysRevB.31.805 (1985).

12 Togo, A. & Tanaka, I. First principles phonon calculations in materials science. *Scripta Materialia* **108**, 1-5, doi:https://doi.org/10.1016/j.scriptamat.2015.07.021 (2015).

13 Allen, P. B., Berlijn, T., Casavant, D. A. & Soler, J. M. Recovering hidden Bloch character: Unfolding electrons, phonons, and slabs. *Physical Review B* **87**, 085322, doi:10.1103/PhysRevB.87.085322 (2013).

14 VandeVondele, J. *et al.* Quickstep: Fast and accurate density functional calculations using a mixed Gaussian and plane waves approach. *Computer Physics Communications* **167**, 103-128, doi:https://doi.org/10.1016/j.cpc.2004.12.014 (2005).

15 Goedecker, S., Teter, M. & Hutter, J. Separable dual-space Gaussian pseudopotentials. *Physical Review B* **54**, 1703-1710, doi:10.1103/PhysRevB.54.1703 (1996).

16 Hartwigsen, C., Goedecker, S. & Hutter, J. Relativistic separable dual-space Gaussian pseudopotentials from H to Rn. *Physical Review B* **58**, 3641-3662, doi:10.1103/PhysRevB.58.3641 (1998).

17 Grimme, S. Accurate description of van der Waals complexes by density functional theory including empirical corrections. *Journal of Computational Chemistry* **25**, 1463-1473, doi:https://doi.org/10.1002/jcc.20078 (2004).

18 Grimme, S. Semiempirical GGA-type density functional constructed with a long-range dispersion correction. *Journal of Computational Chemistry* **27**, 1787-1799, doi:https://doi.org/10.1002/jcc.20495 (2006).

19 Henkelman, G., Uberuaga, B. P. & Jónsson, H. A climbing image nudged elastic band method for finding saddle points and minimum energy paths. *The Journal of Chemical Physics* **113**, 9901-9904, doi:10.1063/1.1329672 (2000).
20 Pulay, P. Convergence acceleration of iterative sequences. the case of scf iteration. *Chemical Physics Letters* **73**, 393-398, doi:https://doi.org/10.1016/0009-2614(80)80396-4 (1980).
21 Momma, K. & Izumi, F. VESTA 3 for three-dimensional visualization of crystal, volumetric and morphology data. *Journal of Applied Crystallography* **44**, 1272-1276, doi:10.1107/S0021889811038970 (2011).
22 Hong, J. *et al.* Exploring atomic defects in molybdenum disulphide monolayers. *Nature Communications* **6**, 6293, doi:10.1038/ncomms7293 (2015).
23 Vancsó, P. *et al.* The intrinsic defect structure of exfoliated MoS2 single layers revealed by Scanning Tunneling Microscopy. *Scientific Reports* **6**, 29726, doi:10.1038/srep29726 (2016).
24 Schulz, F. *et al.* Epitaxial hexagonal boron nitride on Ir(111): A work function template. *Physical Review B* **89**, 235429, doi:10.1103/PhysRevB.89.235429 (2014).
25 Barja, S. *et al.* Identifying substitutional oxygen as a prolific point defect in monolayer transition metal dichalcogenides. *Nature Communications* **10**, 3382, doi:10.1038/s41467-019-11342-2 (2019).
26 Silva, C. C. *et al.* Spatial variation of geometry, binding, and electronic properties in the moiré superstructure of MoS2 on Au(111). *2D Materials* **9**, 025003, doi:10.1088/2053-1583/ac4958 (2022).
27 Popov, I., Seifert, G. & Tománek, D. Designing Electrical Contacts to ${\mathrm{MoS}}_{2}$ Monolayers: A Computational Study. *Physical Review Letters* **108**, 156802, doi:10.1103/PhysRevLett.108.156802 (2012).